Triangular flow in hydrodynamics and transport theory

Triangular flow in hydrodynamics and transport theory

Burak Han Alver,[1] Clément Gombeaud,[2] Matthew Luzum,[2] and Jean-Yves Ollitrault[2,*]
[1]*Laboratory for Nuclear Science, Massachusetts Institute of Technology, Cambridge, Massachusetts 02139-4307, USA*
[2]*CNRS, URA2306, IPhT, Institut de physique theorique de Saclay, F-91191 Gif-sur-Yvette, France*
(Received 2 August 2010; published 30 September 2010)

In ultrarelativistic heavy-ion collisions, the Fourier decomposition of the relative azimuthal angle, $\Delta\phi$, distribution of particle pairs yields a large $\cos(3\Delta\phi)$ component, extending to large rapidity separations $\Delta\eta > 1$. This component captures a significant portion of the ridge and shoulder structures in the $\Delta\phi$ distribution, which have been observed after contributions from elliptic flow are subtracted. An average finite triangularity owing to event-by-event fluctuations in the initial matter distribution, followed by collective flow, naturally produces a $\cos(3\Delta\phi)$ correlation. Using ideal and viscous hydrodynamics and transport theory, we study the physics of triangular (v_3) flow in comparison to elliptic (v_2), quadrangular (v_4), and pentagonal (v_5) flow. We make quantitative predictions for v_3 at RHIC and LHC as a function of centrality and transverse momentum. Our results for the centrality dependence of v_3 show a quantitative agreement with data extracted from previous correlation measurements by the STAR collaboration. This study supports previous results on the importance of triangular flow in the understanding of ridge and shoulder structures. Triangular flow is found to be a sensitive probe of initial geometry fluctuations and viscosity.

DOI: 10.1103/PhysRevC.82.034913 PACS number(s): 25.75.Gz, 25.75.Ld, 24.10.Nz

I. INTRODUCTION

Correlations between particles produced in ultrarelativistic heavy-ion collisions have been thoroughly studied experimentally. Correlation structures previously identified in proton-proton collisions have been observed to be modified and patterns that are specific to nucleus-nucleus collisions have been revealed. The dominant feature in two-particle correlations is elliptic flow, one of the early observations at RHIC [1]. Elliptic flow leads to a $\cos(2\Delta\phi)$ term in the distribution of particle pairs with relative azimuthal angle $\Delta\phi$. More recently, additional structures have been identified in azimuthal correlations after accounting for contributions from elliptic flow [2–7]. An excess of correlated particles is observed in a narrow "ridge" near $\Delta\phi = 0$ and the away-side peak at $\Delta\phi = \pi$ is wider in comparison to that in proton-proton collisions. For central collisions and high-transverse-momentum triggers, the away-side structure develops a dip at $\Delta\phi = \pi$, with two "shoulders" appearing. These ridge and shoulder structures persist for large values of the relative rapidity $\Delta\eta$, which means that they are produced at very early times [8].

It has recently been argued [9] that both the ridge and the shoulder are natural consequences of the triangular flow (v_3) produced by a triangular fluctuation of the initial distribution. The purpose of this paper is to carry out a systematic study of v_3 using relativistic viscous hydrodynamics, which is the standard model for ultrarelativistic heavy-ion collisions [10]. We also perform transport calculations [11], because they allow us to check the range of validity of viscous hydrodynamics and, also, because they provide further insight into the physics. Along with v_3, we also investigate v_4 (quadrangular flow) and v_5 (pentagonal flow). In Sec. II, we recall why odd moments of the azimuthal distributions, such as v_3, are relevant. In Sec. III, we study the general properties of anisotropic flow induced by a harmonic deformation of the initial density profile using hydrodynamics and kinetic theory. In Sec. IV, we present our predictions for v_3 and v_5 at RHIC and LHC. The contribution of quadrangular fluctuations to v_4 is difficult to evaluate because v_4 also has a large contribution from elliptic flow [12]: this will be studied in a forthcoming publication [13].

II. CORRELATIONS FROM FLUCTUATIONS

A fluid at freeze-out emits particles whose azimuthal distribution $f(\phi)$ depends on the distribution of the fluid velocity [12]. $f(\phi)$ can generally be written as a Fourier series,

$$f(\phi) = \frac{1}{2\pi}\left(1 + 2\sum_{n=1}^{+\infty} v_n \cos(n\phi - n\psi_n)\right), \tag{1}$$

where v_n are the coefficients of anisotropic flow [14] that are real and positive, and ψ_n is defined modulo $2\pi/n$ (for $v_n \neq 0$). Equivalently, one can write

$$\langle e^{in\phi}\rangle \equiv \int_0^{2\pi} e^{in\phi} f(\phi)\, d\phi = v_n e^{in\psi_n}, \tag{2}$$

where angle brackets denote an average value over outgoing particles.

Generally, v_n is measured using the event-plane method [15]. However, two-particle correlation measurements are also sensitive to anisotropic flow. Consider a pair of particles with azimuthal angles ϕ_1, $\phi_2 = \phi_1 + \Delta\phi$. Assuming that the only correlation between the particles is caused by the collective expansion, Eq. (2) gives

$$\langle e^{in\Delta\phi}\rangle = \langle e^{in\phi_1} e^{-in\phi_2}\rangle = \langle e^{in\phi_1}\rangle\langle e^{-in\phi_2}\rangle = (v_n)^2. \tag{3}$$

The left-hand side can be measured experimentally, and v_n can thus be extracted from Eq. (3) [16]. Experimentally, one

*jean-yves.ollitrault@cea.fr

averages over several events. v_n fluctuates from one event to the other, and the observable measured through Eq. (3) is the average value of $(v_n)^2$. It can be shown that the event-plane method also measures the rms, $\sqrt{v_n^2}$, unless the "reaction-plane resolution" is extremely good [17,18].

Most fluid calculations of heavy-ion collisions are done with smooth initial profiles [19–23]. These profiles are symmetric with respect to the reaction plane ψ_R, so that all ψ_n in Eq. (1) are equal to ψ_R (with this convention, all v_n are not necessarily positive). For symmetric collisions at midrapidity, smooth profiles are also symmetric under $\phi \to \phi + \pi$, so that all odd harmonics v_1, v_3, etc., are identically 0. However, it has been shown that fluctuations in the positions of nucleons within the colliding nuclei may lead to significant deviations from the smooth profiles event by event [24,25]. They result in lumpy initial conditions that have no particular symmetry, and this lumpiness should be taken into account in fluid dynamical calculations [26–29]. More precisely, one should calculate the azimuthal distribution for each initial condition, then average over initial conditions.

Initial geometry fluctuations are *a priori* important for all v_n, as anticipated in Ref. [30]. Their effect on flow measurements has already been considered for elliptic flow v_2 [31,32] and quadrangular flow v_4 [33]. Event-by-event elliptic flow fluctuations have been measured and found to be significantly large, consistent with the fluctuations in the nucleon positions [34]. Directed flow, v_1, is constrained by transverse momentum conservation, which implies $\sum p_t v_1(p_t) = 0$ and is not considered here. In this paper, we study triangular flow v_3 [9], and pentagonal flow v_5, which arise solely owing to initial geometry fluctuations.

III. FLOW FROM HARMONIC DEFORMATIONS

Elliptic flow is the response of the system to an initial distribution with an elliptic shape in the transverse plane (x, y) [35]. In this article, we study the response to higher-order deformations. For the sake of simplicity, we assume in this section that the initial energy profile in the transverse plane (x, y) is a deformed Gaussian at $t = t_0$:

$$\epsilon(x, y) = \epsilon_0 \exp\left(-\frac{r^2\{1 + \varepsilon_n \cos[n(\phi - \psi_n]\}}{2\rho^2}\right), \quad (4)$$

where we have introduced polar coordinates $x = r\cos\phi$, $y = r\sin\phi$. In Eq. (4), n is a positive integer, ε_n is the magnitude of the deformation, ψ_n is a reference angle, and ρ is the transverse size. Convergence at infinity implies $0 \leqslant \varepsilon_n < 1$. Figure 1 displays contour plots of the energy density for $n = 3$ and $\varepsilon_3 = 0.2$. The sign in front of ε_n in Eq. (4) has been chosen such that ψ_n is the direction of the flat side of the polygon. For $n = 2$, it is the minor axis of the ellipse, which is the standard definition of the participant plane [25].

For $t > t_0$, we assume that the system evolves according to the equations of hydrodynamics or to the Boltzmann transport equation, until particles are emitted, and we compute the azimuthal distribution $f(\phi)$ of outgoing particles. The initial profile, Eq. (4), is symmetric under the transformation $\phi \to \phi + \frac{2\pi}{n}$, therefore $f(\phi)$ has the same symmetry. The only

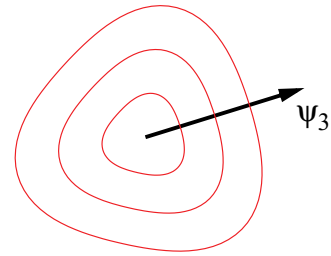

FIG. 1. (Color online) Contour plots of the energy density (4) for $n = 3$ and $\varepsilon_3 = 0.2$.

nonvanishing Fourier coefficients are $\langle e^{in\phi}\rangle$, $\langle e^{2in\phi}\rangle$, $\langle e^{3in\phi}\rangle$, etc. Symmetry of the initial profile under the transformation $(\phi - \psi_n) \to -(\phi - \psi_n)$ implies

$$\langle e^{in\phi}\rangle = v_n e^{in\psi_n}, \quad (5)$$

where v_n is real. As we shall see, v_n is usually positive for $\varepsilon_n > 0$, which means that anisotropic flow develops along the flat side of the polygon (see Fig. 1).

We now present quantitative results for v_n, as defined by Eq. (5), using two models. The first model is relativistic hydrodynamics (see Ref. [10] for details). We fix ϵ_0, t_0, and the freeze-out temperature to the same values as for a central Au-Au collision at RHIC with Glauber initial conditions [10], and $\rho = 3$ fm, corresponding roughly to the rms values of x and y. Unless stated otherwise, results are shown for pions at freeze-out. Corrections owing to resonance decays [36] are not included in this section. They are included only in our final predictions in Sec. IV. The second model is a relativistic Boltzmann equation for massless particles in $2 + 1$ dimensions (see Ref. [11] for details). The only parameter in this calculation is the Knudsen number $K = \lambda/R$, where the mean free path λ and the transverse size R are defined as in Ref. [11]. ρ in Eq. (4) is the rms width of the energy distribution, while R is defined from the rms widths σ_x and σ_y of the *particle* distribution, by $R^{-2} = \sigma_x^{-2} + \sigma_y^{-2}$. For a two-dimensional ideal gas of massless particles, the particle density n is related to the energy density through $n \propto \epsilon^{2/3}$, which gives $R = \frac{\sqrt{3}}{2}\rho$. Boltzmann transport theory is less realistic than hydrodynamics for several reasons.

(i) The equation of state is that of an ideal gas, while the equation of state used in hydrodynamics is taken from lattice QCD: it is much softer around the transition to quark-gluon plasma. Although transport is equivalent to ideal hydrodynamics when the mean free path goes to 0, our results from transport and ideal hydrodynamics differ in this limit, because of the different equation of state.
(ii) There is no longitudinal expansion.
(iii) Particles are massless.

The main advantage of transport theory is that it can be used for arbitrary values of the mean free path, while hydrodynamics can only be used if the mean free path is small. Furthermore, the time evolution of the system can be studied and no modeling is required for the freeze-out process using the

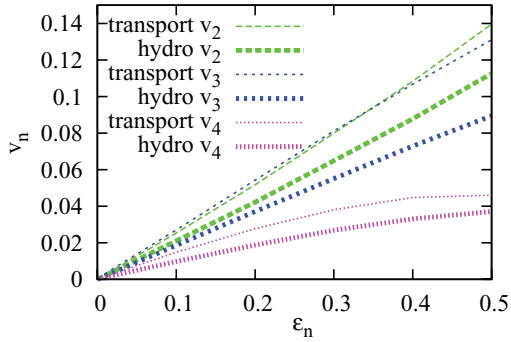

FIG. 2. (Color online) v_n versus ε_n in transport theory and ideal hydrodynamics. The Knudsen number in the transport calculation is $K = 0.025$, close to the ideal hydrodynamics limit $K = 0$.

transport approach, because one follows all elastic collisions until the very last one.

A. v_n versus ε_n

Figure 2 displays v_n versus ε_n for $n = 2, 3, 4$ in transport theory and ideal hydrodynamics (zero viscosity). The values of v_n are smaller in hydrodynamics, which is caused by the softer equation of state [37].

As expected from previous studies of v_2 [38] and v_3 [9], we observe that v_n is linear for small values of ε_n. Nonlinearities are stronger for larger values of n, in both transport theory and hydrodynamics. A possible interpretation of these strong nonlinearities is that the contour plot of the initial density is no longer convex if $\varepsilon_n > 2/(n^2 - 2)$. The threshold values for $n = 3, 4$ are $\varepsilon_3 = \frac{2}{7}$ and $\varepsilon_4 = \frac{1}{7}$. If the contour plot is not convex, the streamlines (which are orthogonal to equal density contours) are no longer divergent: shock waves may appear, which hinder the development of anisotropies.

The results presented in the remainder of this section are obtained in the linear regime where $v_n \propto \varepsilon_n$. In this regime, we find $v_2/\varepsilon_2 \simeq 0.21$, in agreement with other calculations [39]. Note that in our hydrodynamic calculation, chemical equilibrium is maintained until freeze-out. When chemical freeze-out is implemented earlier than kinetic freeze-out, v_2/ε_2 is slightly larger [19]. Figure 2 shows that v_3/ε_3 has a magnitude comparable to that of v_2/ε_2, while v_4/ε_4 is significantly smaller. Our results for v_5/ε_5 (not shown) are even smaller.

B. Time dependence

In the transport approach, one follows all the trajectories of the particles, so that v_n is well defined at all times, which is not the case in hydrodynamics before freeze-out. Figure 3 displays the results for v_n versus t/ρ, where ρ is the width of the initial distribution, Eq. (4). As expected for dimensional reasons [37], anisotropic flow appears for $t \sim \rho$. However, v_n appears slightly later for larger n. This can be traced to the behavior of v_n at early times. The transport results presented in Fig. 3 are obtained with a very small value of the Knudsen number, $K = 0.025$, close to the ideal hydrodynamics limit. In ideal fluid dynamics, the fluid transverse velocity increases linearly with t, and v_n involves an nth power of the fluid velocity, so that v_n scales like t^n. In transport theory, the

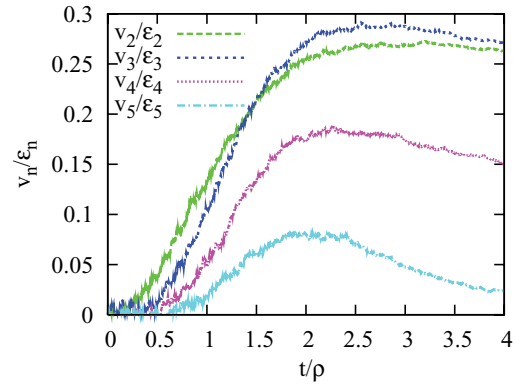

FIG. 3. (Color online) v_n/ε_n versus time in transport theory. Each curve is the result of a single Monte Carlo simulation with $K = 0.025$ and $\varepsilon_n = 0.1$. The number of particles in the simulation is $N = 4 \times 10^6$, and the corresponding statistical error in v_n/ε_n is 3.5×10^{-3}.

number of collisions increases like t at early times, which gives an extra power of t, and v_n increases like t^{n+1} [11]. In both cases, the behavior of v_n at small t is flatter for larger values of n, which is clearly shown in Fig. 3.

While elliptic flow keeps increasing with time (it decreases slightly at later times, not shown in Fig. 3), v_n with $n \geqslant 3$ reaches a maximum and then decreases. The decrease is more pronounced for larger n: the mechanism producing v_n is self-quenching.

C. Differential flow

Figure 4 displays the differential anisotropic flow $v_n(p_t)$ versus the transverse momentum p_t for pions in ideal hydrodynamics, scaled by the initial eccentricity ε_n. At low p_t, one generally expects v_n to scale like $(p_t)^n$ for massive particles [40].[1] One clearly sees that v_n is much flatter at low p_t for larger values of n. For larger values of p_t, $v_n(p_t)$ is linear in p_t. The arguments that explain this linear dependence of v_2 [12] can be generalized to arbitrary n [41]. The linear

[1]There is no such constraint for massless particles where the $p_t \to 0$ limit is singular. Our transport calculations for massless partons give $v_n(p_t) \propto p_t$ at low p_t for all n.

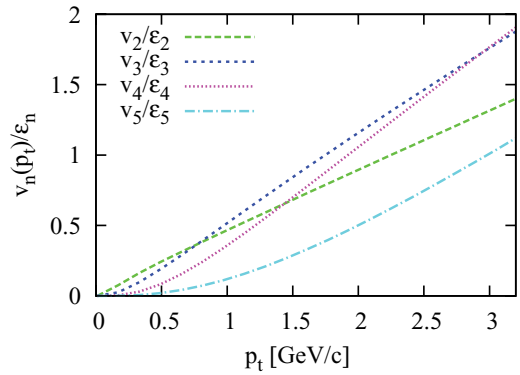

FIG. 4. (Color online) v_n/ε_n versus p_t in ideal hydrodynamics, with $\varepsilon_n = 0.1$.

behavior at larger p_t is also clearly shown in Fig. 4. It has already been noted for v_3 [9].

The value of v_3 increases with p_t, which explains why the ridge and shoulder are more pronounced with a high p_t trigger ("hard" ridge) [42]. Though the relative strength of v_3 is smaller at low p_t, it is still comparable to v_2, leading to the smaller "soft" ridge [43]. Predictions for $v_3(p_t)$ in viscous hydrodynamics for identified particles are presented in Sec. IV.

D. Viscous damping of v_n

We study the effect of viscosity first in the transport approach, then in viscous hydrodynamics. In transport, the degree of thermalization is characterized by the Knudsen number K. Experimentally, $1/K$ scales like $(1/S)(dN/dy)$, where dN/dy is the multiplicity per unit rapidity, and S is the overlap area between the colliding nuclei [44]. The dependence of v_n on K can be studied by varying the collision system and the centrality of the collision [45].

Transport is equivalent to ideal hydrodynamics in the limit $K \to 0$. For small K, observables (such as v_n and particle spectra) deviate from the $K = 0$ limit by corrections that are linear in K. These are the viscous corrections: both K and the shear viscosity η are proportional to the particle mean free path λ. Viscous damping is expected to scale with the wave number k like k^2. Here, the wavelength of the deformation is $2\pi R/n$; hence, $k \sim n/R$. Therefore viscous corrections should scale with K and n approximately like n^2K [46]. The limit $K \to \infty$ (free streaming) is also interesting, as v_n vanishes in this limit. For large K, one therefore expects v_n to scale like $1/K$, which is essentially the number of collisions per particle [11]. For intermediate values of K ($K \sim 1$), no universal behavior is expected, and observables depend on the scattering cross section used in the transport calculation (dependence on energy and scattering angle).

Figure 5 displays the variation of v_n/ε_n versus the scaling variable $1/(n^2K)$ in the transport calculation. Our numerical results can be fitted by smooth rational functions (Padé approximants) [47] for all K:

$$v_n(K) = v_n^{\text{ih}} \frac{1 + B_n K + D_n K^2}{1 + (A_n + B_n)K + C_n K^2 + E_n K^3}, \tag{6}$$

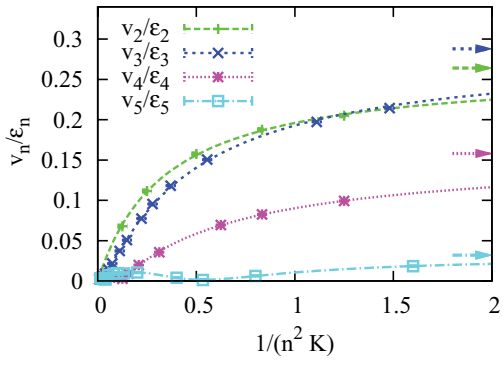

FIG. 5. (Color online) v_n/ε_n versus $1/(n^2K)$ in transport theory. Values of ε_n are $\varepsilon_2 = \frac{5}{13}$, $\varepsilon_3 = \varepsilon_4 = 0.3$, and $\varepsilon_5 = 0.1$. Arrows indicate our extrapolation to $K = 0$ (ideal hydrodynamics limit) using Eq. (6).

where v_n^{ih}, A_n, B_n, C_n, D_n, and E_n are fit parameters. This formula has the expected behavior in both $K \to 0$ and $K \to \infty$ limits. For $n = 2$, the lowest-order formula, with $B_2 = C_2 = D_2 = E_2 = 0$, gives a good fit [11]. For $n = 3$, we obtain a good fit using the next-to-leading-order approximant, with $D_3 = E_3 = 0$ but free B_3, C_3. For $n = 4$ or 5, we need all six parameters to achieve a good fit. Fits are represented as solid lines in Fig. 5, and extrapolations to $K = 0$ are indicated by arrows. As already noted, the hydrodynamics limits $v_3^{\text{ih}}/\varepsilon_3$ and $v_2^{\text{ih}}/\varepsilon_2$ are comparable, while $v_4^{\text{ih}}/\varepsilon_4$ is smaller by roughly a factor of 2. $v_5^{\text{ih}}/\varepsilon_5$ is found to be smaller yet by about a factor 5, with a large theoretical uncertainty.

For small K, $v_n(K) \simeq v_n^{\text{ih}}(1 - A_n K)$: the parameter A_n measures the magnitude of the viscous correction. Our fit gives $A_2 = 1.4 \pm 0.1$ [11], $A_3 = 4.2 \pm 0.3$, and $A_4 = 11.0 \pm 0.9$. The error bar on A_5 is too large to extract a meaningful value. For $n = 2, 3, 4$, we observe $A_n \propto n^\alpha$ with $\alpha = 2.8 \pm 0.2$, closer to n^3 than to the expected n^2. The fact that viscous corrections are larger for larger n also implies that the range of validity of viscous hydrodynamics is smaller for v_n with $n \geqslant 3$ than for v_2. Even after rescaling K by n^2, corrections are linear in K only for very small K, which is why higher-order Padé approximations are needed.

The magnitude of viscous effects can be seen more directly by varying the shear viscosity η in viscous hydrodynamics [48]. For each value of n, we have performed three calculations, with $\eta \simeq 0$ (ideal hydrodynamics), $\eta/s = 0.08 \simeq 1/4\pi$ [49], and $\eta/s = 0.16$, where s is the entropy density. The result is presented in Fig. 6. The variation of v_n with η is found to be linear for all n for this range of viscosities, which is a hint that viscous hydrodynamics (which addresses first-order deviations to local equilibrium) is a reasonable description. Interestingly, the lines are almost parallel, which means that the absolute viscous correction to v_n/ε_n depends little on n. However, as v_n/ε_n is smaller for larger n, the *relative* viscous correction is larger for larger n. From the transport calculation, we expect that the relative viscous correction is 3 times larger for v_3 than for v_2 and 8 times larger for v_4 than for v_2. The increase in Fig. 6 is more modest. Note that we keep the freeze-out temperature constant for all values of η/s. Strictly speaking, this is inconsistent. Freeze-out is

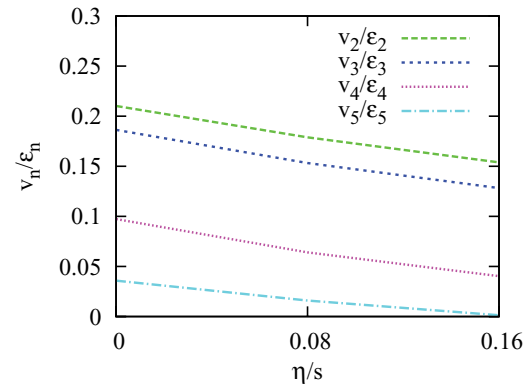

FIG. 6. (Color online) v_n/ε_n versus η/s in hydrodynamics. The initial and freeze-out temperature are $T_i = 340$ MeV and $T_f = 140$ MeV, respectively.

defined as the point where viscous corrections become so large that hydrodynamics breaks down: when the viscosity goes to 0, so does the freeze-out temperature [12]. By varying only η/s and keeping T_f constant, we only capture part of the viscous correction.[2] Because triangular flow, like elliptic flow, develops at early times, v_3 is sensitive to the value of η/s at the high-density phase of the collision.

IV. PREDICTIONS FOR v_3 AT RHIC AND LHC

A. Triangularity fluctuations

We now give realistic predictions for v_3 at RHIC and LHC. The transport calculations in Ref. [9] show that, even with lumpy initial conditions, v_3 in a given event scales like the triangularity ε_3. We define ε_n as in [9]:

$$\varepsilon_n e^{\mathrm{in}\psi_n} \equiv -\frac{\int \epsilon(x,y)\, r^2 e^{\mathrm{in}\phi}\, dx\, dy}{\int \epsilon(x,y)\, r^2\, dx\, dy}, \tag{7}$$

where $\epsilon(x,y)$ is the initial energy density and (r,ϕ) are the usual polar coordinates, $x = r\cos\phi$, $y = r\sin\phi$.

Following the discussion in Sec. II, experiments measure the average value of $(v_n)^2$, so that

$$v_n^{\mathrm{exp}} = \sqrt{\langle (v_n)^2 \rangle}. \tag{8}$$

Assuming $v_n = \kappa\varepsilon_n$ in each event, the measured v_n scales like the rms ε_n defined by

$$\varepsilon_n^{\mathrm{rms}} \equiv \sqrt{\langle (\varepsilon_n)^2 \rangle}. \tag{9}$$

We compute $\varepsilon_n^{\mathrm{rms}}$ using two different models. The first model is the PHOBOS Monte Carlo Glauber model [50], where it is assumed that the initial energy is distributed in the transverse plane in the same way as nucleons within colliding nuclei. We modify the initial model slightly [33] by giving each nucleon a weight $w = 1 - x + xN_{\mathrm{coll}}$, where N_{coll} is the number of binary collisions of the nucleon. We take $x = 0.145$ at RHIC and $x = 0.18$ at the LHC [51]. The second model is the Monte Carlo KLN model of Drescher and Nara [52], which is the only model incorporating both saturation physics and fluctuations. Both of these models yield event-by-event eccentricity fluctuations, which are consistent with measured elliptic flow fluctuations [34]. We loosely refer to the two models as Glauber and color glass condensate (CGC).

Figure 7 displays $\varepsilon_n^{\mathrm{rms}}$ as a function of the number of participants. $\varepsilon_2^{\mathrm{rms}}$ is larger than $\varepsilon_{3,4,5}^{\mathrm{rms}}$ for noncentral collisions, which is caused by the almond shape of the overlap area. The eccentricity is somewhat larger with CGC than Glauber [54]. $\varepsilon_3^{\mathrm{rms}}$ is very close to $\varepsilon_5^{\mathrm{rms}}$. Both vary with N_{Part} essentially like $(N_{\mathrm{Part}})^{-1/2}$, as generally expected for statistical fluctuations [55]. Unlike $\varepsilon_2^{\mathrm{rms}}$, they are slightly *smaller* for CGC than for Glauber. Because the only source of fluctuations that is considered in both models is the position of the nucleons in the colliding nuclei, this difference may be caused by the technical implementation of the Monte Carlo KLN model.

[2]We have checked that v_3/ε_3 is larger with a lower freeze-out temperature $T_f = 100$ MeV. In particular, we find $v_3/\varepsilon_3 > v_2/\varepsilon_2$, in agreement with the transport calculation.

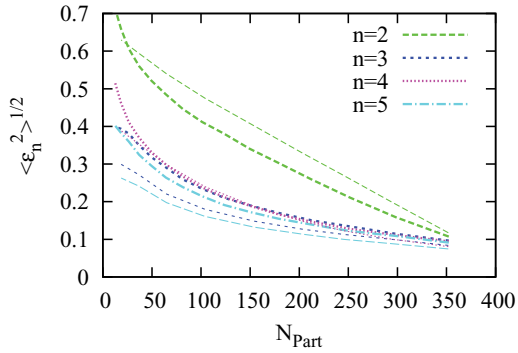

FIG. 7. (Color online) Root mean square eccentricities $\varepsilon_n^{\mathrm{rms}}$ for $n = 2, 3, 4, 5$ for Au-Au collisions at 200 GeV per nucleon, versus the number of participant nucleons N_{Part}. N_{Part} is used as a measure of the centrality in nucleus-nucleus collisions: it is largest for central collisions, with zero impact parameter [53]. Thick lines, Monte Carlo Glauber model [50]; thin lines, Monte Carlo KLN model [52].

Finally, $\varepsilon_4^{\mathrm{rms}}$ is slightly larger than odd harmonics for peripheral collisions because the almond shape induces a nonzero ε_4 as a second-order effect. Figure 7 only displays results for Au-Au collisions at RHIC. Results for Pb-Pb collisions at the LHC are similar, except for the different range in N_{part} and the somewhat larger difference between Glauber and CGC for ε_3.

B. Method for obtaining v_3 in hydrodynamics

To make predictions for v_3, we start from a smooth initial energy profile $\epsilon(r,\phi)$, possessing the usual symmetries $\phi \to -\phi$ and $\phi \to \phi + \pi$. By hand, we then put a $\cos(3\phi)$ deformation through the transformation, inspired by Eq. (4),

$$\epsilon(r,\phi) \to \epsilon(r\sqrt{1 + \varepsilon_3' \cos[3(\phi - \psi_3')]}, \phi), \tag{10}$$

where ε_3' is the magnitude of the deformation, and ψ_3' the flat axis of the triangle. We choose $\varepsilon_3' = \varepsilon_3^{\mathrm{rms}}$. The choice of ψ_3' is arbitrary. The initial profile has a nonzero eccentricity for noncentral collisions, owing to the almond shape of the overlap area. Through Eq. (10), we add a triangular deformation to an ellipse. Because the original profile has $\phi \to \phi + \pi$ symmetry, ψ_3' is equivalent to $\psi_3' + \frac{\pi}{3}$. Furthermore, ψ_3' is equivalent to $-\psi_3'$, owing to $\phi \to -\phi$ symmetry. Therefore, one need only vary ψ_3' between 0 and $\frac{\pi}{6}$. We choose the values 0, $\frac{\pi}{12}$, and $\frac{\pi}{6}$.

We then compute ε_3 and ψ_3 defined by Eq. (7). With the Gaussian profile, Eq. (4), the input and output values are identical: $\varepsilon_3' = \varepsilon_3$, $\psi_3' = \psi_3$. Our predictions use two sets of profiles, which both describe RHIC data well [10]: optical Glauber and (fKLN) CGC. With both profiles, ε_3' differs from ε_3 by a few percent. ψ_3 is essentially identical to ψ_3', which means that the elliptic deformation does not interfere with the triangular deformation. According to the previous discussion, we should tune ε_3' in such a way that $\varepsilon_3 = \varepsilon_3^{\mathrm{rms}}$ to make predictions for v_3. It is, however, easier to use the proportionality between v_3 and ε_3: one can then do the calculation for an arbitrary ε_3' and rescale the final results by $\varepsilon_3^{\mathrm{rms}}/\varepsilon_3$. We use $\varepsilon_3^{\mathrm{rms}}$ from the Monte Carlo Glauber model with Glauber initial conditions and from the Monte Carlo KLN model with CGC initial conditions.

There is some arbitrariness in the definition of the triangularity ε_3: one could, for instance, replace r^2 with r^3 in Eq. (7) [56]. With this replacement, both ε_3 and $\varepsilon_3^{\rm rms}$ (from the Monte Carlo calculations) increase, but the ratio $\varepsilon_3^{\rm rms}/\varepsilon_3$—and therefore also our predicted v_3—changes little (less than 7% for all centralities and both sets of initial conditions).[3]

Finally, we compute v_3 in viscous hydrodynamics. It has been shown that RHIC data are fit equally well with Glauber initial conditions and $\eta/s = 0.08$ and with CGC initial conditions and $\eta/s = 0.16$ [10]. The larger eccentricity of CGC (which should produce more elliptic flow) is compensated by the higher viscosity (larger damping and less flow), so that the final values of v_2 are very similar. For LHC energies, details are as in Ref. [57] (with v_3 calculated from a Cooper-Frye freeze-out prescription). In all cases, v_3 is found to be independent of the orientation of the triangle ψ_3'. In the case of Glauber initial conditions, we perform calculations of v_3 with and without resonance decays at freeze-out [36]. Resonance decays roughly amount to multiplying v_3 by 0.75 at RHIC and by 0.83 at the LHC. Our CGC results are computed without resonance decays and multiplied by the same factor at the end of the calculation.

C. Results and comparison with data

Results are displayed in Fig. 8 for both sets of initial conditions. CGC initial conditions have both a smaller triangularity and a higher viscosity, so that they predict a much smaller v_3. The change in viscosity explains roughly 70% of the difference between CGC and Glauber at RHIC, and about half at the LHC. The centrality dependence is much flatter in Fig. 8 than in Fig. 7. The decrease in $\varepsilon_3^{\rm rms}$ with increasing $N_{\rm Part}$ is compensated by the increase in the system size and lifetime, which leads to a smaller effective Knudsen number K or, equivalently, a smaller viscous correction. We predict values of v_3 significantly larger at the LHC than at RHIC. This is because viscous damping is less important, owing to the larger lifetime of the fluid at LHC [57].

[3]If one replaces r^2 with r^k in Eq. (7), ε_n scales with k like $k+2$ for a smooth, symmetric density profile $\epsilon(r)$ deformed according to Eq. (10). Therefore, ε_3 is larger by $\frac{5}{4}$ if defined with a factor of r^3 instead of r^2.

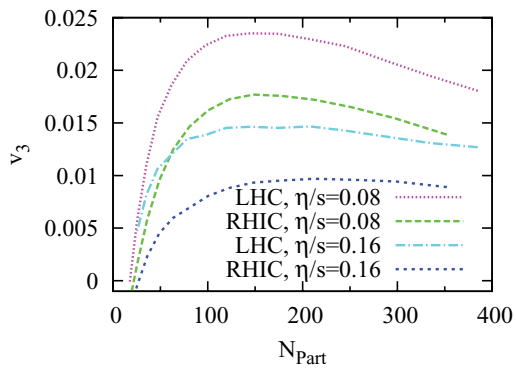

FIG. 8. (Color online) Average v_3 of pions as a function of the number of participants for Au-Au collisions at 200 GeV per nucleon (RHIC) and Pb-Pb collisions at 5.5 TeV per nucleon (LHC). Hydrodynamic predictions are for Glauber initial conditions with $\eta/s = 0.08$ and CGC initial conditions with $\eta/s = 0.16$, which best fit v_2 data at the RHIC [10].

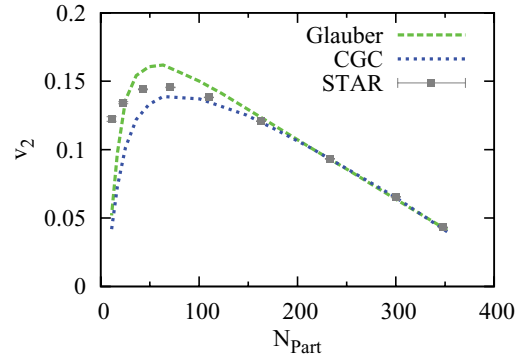

FIG. 9. (Color online) v_2 for charged particles with $0.8 < p_t < 4$ GeV/c extracted from STAR charge-independent correlation data [4] and predictions from viscous hydrodynamics [10] with Glauber initial conditions and $\eta/s = 0.08$ or CGC initial conditions with $\eta/s = 0.16$. Theoretical calculations are for pions with the same p_t cutoff as the data and are scaled by the rms eccentricity from the corresponding Monte Carlo model. See text for details.

Although experimental data for triangular flow are not yet available, both v_2 and v_3 can be extracted from the measured two-particle azimuthal correlation using Eq. (3) [9]. Figures 9 and 10 display a comparison between experimental data from STAR [4] and our hydrodynamic calculations. The STAR data are obtained from correlations between particles at midrapidity ($|\eta| < 1$) and intermediate transverse momentum ($0.8 < p_t < 4.0$ GeV). The correlation results have been projected at $1.2 < \Delta\eta < 1.9$ to reduce the sensitivity to nonflow effects.

We first discuss our results for v_2. As already explained, our hydrodynamic model has smooth initial conditions and does not include the effect of eccentricity fluctuations for v_2. Because $v_2 \propto \varepsilon_2$ to a good approximation, we have rescaled our result for v_2 by the rms ε_2 in Fig. 7 (again using the Monte Carlo Glauber for Glauber initial conditions and the Monte Carlo KLN for CGC). This rescaling significantly improves the agreement with data, compared to that in Ref. [10], for the most central bin. As shown in Fig. 9, the agreement between theory and data is excellent with both sets of initial conditions.

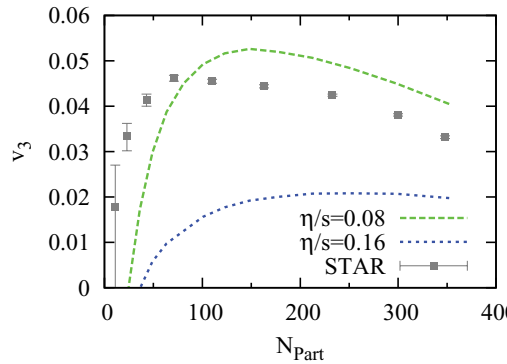

FIG. 10. (Color online) Same as Fig. 9, for v_3.

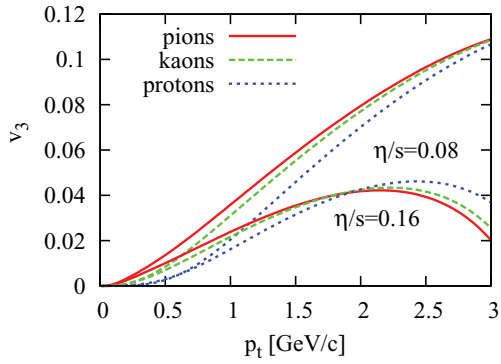

FIG. 11. (Color online) Differential triangular flow for identified particles in central (0–5%) Au-Au collisions at RHIC.

The lower viscosity associated with Glauber initial conditions results in a somewhat steeper centrality dependence than for CGC initial conditions.

Results for v_3 are shown in Fig. 10. The larger magnitude, compared to that in Fig. 8, is caused by the low p_t cutoff. The cutoff also enhances the effect of viscosity, resulting in a larger difference between Glauber and CGC. With a low p_t cutoff, the viscous correction is mostly caused by the distortion of the momentum distribution at freeze-out [58]. The momentum dependence of this distortion is strongly model dependent [59]. The present calculation uses the standard quadratic ansatz, which may overestimate the viscous correction at large p_t [60]. The magnitude and the centrality dependence of v_3 observed by STAR are rather well reproduced by our calculation with Glauber initial conditions, except for peripheral collisions, where hydrodynamics is not expected to be valid.

Figure 11 displays our predictions for $v_3(p_t)$ of identified particles at RHIC. As anticipated in Ref. [41], the well-known mass ordering of elliptic flow [61] is also expected for v_3. At high p_t, a strong viscous suppression is observed. As already explained, the p_t dependence of the viscous correction is model dependent, and it is likely that the quadratic ansatz used here overestimates the viscous corrections at large p_t [60]. Note that effects of resonance decays are not included in Fig. 11. Resonance decays change the results only slightly in the low-p_t region.

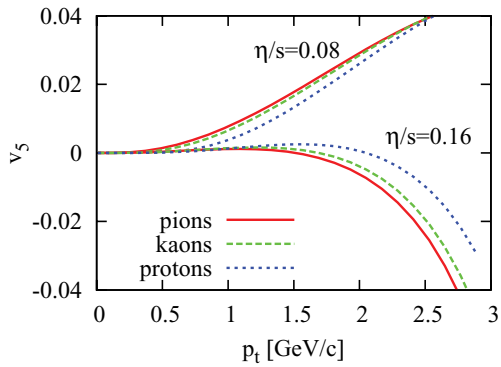

FIG. 12. (Color online) Differential pentagonal flow for identified particles in central (0–5%) Au-Au collisions at the RHIC.

Finally, we have also computed v_5 along the same lines as v_3. The driving force for v_5 is the rms ε_5, which is very close to ε_3 (see Fig. 7). However, the hydrodynamic response is much smaller, and viscous damping is also much larger as discussed in Sec. III. We find that the average integrated v_5 is smaller than v_3 by at least a factor of 10. Results for differential v_5 are presented in Fig. 12. v_5 varies more strongly with p_t than do v_2 and v_3, and it becomes as large as 0.02 at $p_t = 1.5$ GeV/c if η/s is as small as 0.08. For higher viscosities, however, v_5 may be too small to measure even with a high p_t trigger.

V. CONCLUSIONS

We have presented a systematic study of triangular flow in ideal and viscous hydrodynamics and transport theory. Triangular flow is driven by the average event-by-event triangularity in the transverse distribution of nucleons, in the same way that elliptic flow is driven by the initial eccentricity of this distribution. The physics of v_3 is, in many respects, similar to the physics of v_2. In ideal hydrodynamics, the response to the initial deformation is almost identical in both harmonics: $v_3/\varepsilon_3 \simeq v_2/\varepsilon_2 \simeq 0.2$. For quadrangular flow, v_4/ε_4 is smaller, typically by a factor of 2. For pentagonal flow, v_5/ε_5 is so small that v_5 is unlikely to be measurable, even though ε_3 and ε_5 are almost equal. v_3 develops slightly more slowly than v_2, though over comparable time scales. The dependence on transverse momentum p_t is similar for v_3 and v_2, but v_3/v_2 increases with p_t. Hydrodynamics predicts a similar mass ordering for $v_3(p_t)$ and $v_2(p_t)$: v_3 at fixed p_t is smaller for more massive particles. These results can be checked experimentally by a differential measurement of triangular flow.

We have also made predictions for triangular flow, v_3, at RHIC and LHC, using viscous hydrodynamics. Using as input the triangularity from a standard Monte Carlo Glauber model, and a viscosity $\eta/s = 0.08$, we reproduce both the magnitude (within 20%) and the centrality dependence of v_3 extracted from STAR correlation measurements, without any adjustable parameter. Our results support the hypothesis made in Ref. [9] that triangular flow explains most of the ridge and shoulder structures observed in the two-particle azimuthal correlation.

Triangular flow is a sensitive probe of viscosity. Viscous effects drive the energy and centrality dependence of v_3. More central collisions have fewer fluctuations and, hence, smaller triangularity. This decrease is, to a large extent, compensated by the increase in the system size and lifetime, resulting in a very slow decrease in v_3 with centrality (except for peripheral collisions, where viscous hydrodynamics is unlikely to be valid). Comparison with existing data favors a low value of η/s. At the LHC, smaller viscous corrections are expected, owing to the increased lifetime of the fluid: we predict that v_3 should be larger than at RHIC, typically by a factor of $\frac{4}{3}$.

The absolute value of v_3 scales linearly with the average initial triangularity. We have used two models of initial geometry that incorporate fluctuations, the Monte Carlo Glauber model and the Monte Carlo KLN model. The underlying source of fluctuations is the same in both of these models. More work is needed to constrain initial fluctuations on the theoretical side. More work is also needed to incorporate these fluctuations

more readily into hydrodynamic calculations. Although triangular flow is expected to be created by lumpy initial conditions, our predictions are based on smooth initial conditions, in the same spirit as the study of transverse momentum fluctuations in Ref. [22]. The underlying assumption is that v_3/ε_3 is the same for lumpy initial conditions and for smooth initial conditions. The validity of this assumption should eventually be checked.

Triangular flow is a new observable that should be used to constrain models of heavy-ion collisions, along with elliptic flow. Elliptic flow depends on initial eccentricity, fluctuations, and viscosity, which are poorly constrained theoretically. Triangular flow depends solely on fluctuations and viscosity, with a stronger sensitivity to viscosity than v_2. Two different sets of initial conditions, which fit v_2 data equally well, give very different results for v_3. Experiments could measure v_3 as a function of transverse momentum, system size, and centrality. As shown in this paper, theoretical predictions for the dependence of v_3 on these parameters are very specific. If experiments confirm our predictions, simultaneous analyses of v_2 and v_3 can be used to improve our understanding of the initial geometry of heavy-ion collisions and to pin down the viscosity of hot QCD.

ACKNOWLEDGMENTS

This work was funded by the Agence Nationale de la Recherche under Grant No. ANR-08-BLAN-0093-01 and by US Department of Energy (DOE) Grant No. DE-FG02-94ER40818. We thank S. Gavin, T. Hirano, P. Huovinen, and A. Poskanzer for stimulating discussions and W. Zajc for useful comments on the manuscript. M.L. and J.-Y.O. thank the organizers of the program "Quantifying the Properties of Hot QCD Matter" and the Institute for Nuclear Theory at the University of Washington, where part of this work was done, for its hospitality, and the DOE for partial support.

[1] K. H. Ackermann *et al.* (STAR Collaboration), Phys. Rev. Lett. **86**, 402 (2001).
[2] A. Adare *et al.* (PHENIX Collaboration), Phys. Rev. C **78**, 014901 (2008).
[3] B. I. Abelev *et al.* (STAR Collaboration), Phys. Rev. Lett. **102**, 052302 (2009).
[4] B. I. Abelev *et al.* (STAR Collaboration), arXiv:0806.0513 [nucl-ex].
[5] B. Alver *et al.* (PHOBOS Collaboration), Phys. Rev. C **81**, 024904 (2010).
[6] B. Alver *et al.* (PHOBOS Collaboration), Phys. Rev. Lett. **104**, 062301 (2010).
[7] B. I. Abelev *et al.* (STAR Collaboration), Phys. Rev. C **80**, 064912 (2009).
[8] A. Dumitru, F. Gelis, L. McLerran, and R. Venugopalan, Nucl. Phys. A **810**, 91 (2008).
[9] B. Alver and G. Roland, Phys. Rev. C **81**, 054905 (2010).
[10] M. Luzum and P. Romatschke, Phys. Rev. C **78**, 034915 (2008); **79**, 039903(E) (2009).
[11] C. Gombeaud and J. Y. Ollitrault, Phys. Rev. C **77**, 054904 (2008).
[12] N. Borghini and J. Y. Ollitrault, Phys. Lett. B **642**, 227 (2006).
[13] M. Luzum, C. Gombeaud, and J.-Y. Ollitrault (in preparation).
[14] S. Voloshin and Y. Zhang, Z. Phys. C **70**, 665 (1996).
[15] A. M. Poskanzer and S. A. Voloshin, Phys. Rev. C **58**, 1671 (1998).
[16] S. Wang *et al.*, Phys. Rev. C **44**, 1091 (1991).
[17] J. Y. Ollitrault, A. M. Poskanzer, and S. A. Voloshin, Phys. Rev. C **80**, 014904 (2009).
[18] B. Alver *et al.*, Phys. Rev. C **77**, 014906 (2008).
[19] P. Huovinen, Eur. Phys. J. A **37**, 121 (2008).
[20] T. Hirano and Y. Nara, Phys. Rev. C **79**, 064904 (2009).
[21] H. Song and U. W. Heinz, Phys. Rev. C **81**, 024905 (2010).
[22] W. Broniowski, M. Chojnacki, and L. Obara, Phys. Rev. C **80**, 051902 (2009).
[23] P. Bozek, Phys. Rev. C **81**, 034909 (2010).
[24] M. Miller and R. Snellings, arXiv:nucl-ex/0312008.
[25] S. Manly *et al.* (PHOBOS Collaboration), Nucl. Phys. A **774**, 523 (2006).
[26] M. Gyulassy, D. H. Rischke, and B. Zhang, Nucl. Phys. A **613**, 397 (1997).
[27] O. J. Socolowski, F. Grassi, Y. Hama, and T. Kodama, Phys. Rev. Lett. **93**, 182301 (2004).
[28] H. Holopainen, H. Niemi, and K. J. Eskola, arXiv:1007.0368.
[29] K. Werner, I. Karpenko, T. Pierog, M. Bleicher, and K. Mikhailov, arXiv:1004.0805.
[30] A. P. Mishra, R. K. Mohapatra, P. S. Saumia, and A. M. Srivastava, Phys. Rev. C **77**, 064902 (2008).
[31] R. Andrade, F. Grassi, Y. Hama, T. Kodama, and O. J. Socolowski, Phys. Rev. Lett. **97**, 202302 (2006).
[32] B. Alver *et al.* (PHOBOS Collaboration), Phys. Rev. Lett. **98**, 242302 (2007).
[33] C. Gombeaud and J. Y. Ollitrault, Phys. Rev. C **81**, 014901 (2010).
[34] B. Alver *et al.* (PHOBOS Collaboration), Phys. Rev. C **81**, 034915 (2010).
[35] J. Y. Ollitrault, Phys. Rev. D **46**, 229 (1992).
[36] J. Sollfrank, P. Koch, and U. W. Heinz, Z. Phys. C **52**, 593 (1991).
[37] R. S. Bhalerao, J. P. Blaizot, N. Borghini, and J. Y. Ollitrault, Phys. Lett. B **627**, 49 (2005).
[38] H. Sorge, Phys. Rev. Lett. **82**, 2048 (1999).
[39] P. Huovinen and T. Hirano (private communication).
[40] P. M. Dinh, N. Borghini, and J. Y. Ollitrault, Phys. Lett. B **477**, 51 (2000).
[41] A. P. Mishra, R. K. Mohapatra, P. S. Saumia, and A. M. Srivastava, Phys. Rev. C **81**, 034903 (2010).
[42] J. Putschke, J. Phys. G **34**, S679 (2007).
[43] M. Daugherity (for the STAR Collaboration), J. Phys. G **35**, 104090 (2008).
[44] H. J. Drescher, A. Dumitru, C. Gombeaud, and J. Y. Ollitrault, Phys. Rev. C **76**, 024905 (2007).
[45] S. A. Voloshin and A. M. Poskanzer, Phys. Lett. B **474**, 27 (2000).
[46] S. Gavin (private communication).
[47] J. L. Nagle, P. Steinberg, and W. A. Zajc, Phys. Rev. C **81**, 024901 (2010).
[48] U. W. Heinz, J. S. Moreland, and H. Song, Phys. Rev. C **80**, 061901 (2009).

[49] P. K. Kovtun, D. T. Son, and A. O. Starinets, Phys. Rev. Lett. **94**, 111601 (2005).
[50] B. Alver, M. Baker, C. Loizides, and P. Steinberg, arXiv:0805.4411 [nucl-ex].
[51] P. Bozek, M. Chojnacki, W. Florkowski, and B. Tomasik, arXiv:1007.2294 [unknown].
[52] H. J. Drescher and Y. Nara, Phys. Rev. C **76**, 041903 (2007).
[53] M. L. Miller, K. Reygers, S. J. Sanders, and P. Steinberg, Annu. Rev. Nucl. Part. Sci. **57**, 205 (2007).
[54] T. Lappi and R. Venugopalan, Phys. Rev. C **74**, 054905 (2006).
[55] R. S. Bhalerao and J. Y. Ollitrault, Phys. Lett. B **641**, 260 (2006).
[56] Y. Li and D. Teaney (in preparation); D. Teaney, presented at Strong and Electroweak Matter 2010, Montreal, Canada, June 29–July 2.
[57] M. Luzum and P. Romatschke, Phys. Rev. Lett. **103**, 262302 (2009).
[58] D. Teaney, Phys. Rev. C **68**, 034913 (2003).
[59] K. Dusling, G. D. Moore, and D. Teaney, Phys. Rev. C **81**, 034907 (2010).
[60] M. Luzum and J. Y. Ollitrault, Phys. Rev. C **82**, 014906 (2010).
[61] P. Huovinen, P. F. Kolb, U. W. Heinz, P. V. Ruuskanen, and S. A. Voloshin, Phys. Lett. B **503**, 58 (2001).